Journal of
Composites Science

MDPI

Article

Experimental Evaluation of Induction- and Conduction-Welded Thermoplastic Composite Single-Lap Shear Joints

Arne Schiller [1] and Chiara Bisagni [1,2,*]

[1] Department of Aerospace Structures and Materials, Delft University of Technology, 2629 HS Delft, The Netherlands; a.schiller@tudelft.nl
[2] Department of Aerospace Science and Technology, Politecnico di Milano, 20156 Milan, Italy
* Correspondence: chiara.bisagni@polimi.it

Abstract

Single-lap shear joints made from fabric T300/polyphenylene sulfide (T300/PPS) and unidirectional T700/low-melt polyaryletherketone (T700/LM-PAEK) laminates are joined via induction and conduction welding at different processing temperatures. The joints are tested experimentally to investigate the influence of the processing temperature on the damage evolution in the specimens which is tracked using digital image correlation. Cracks grow rapidly in the unwelded parts of the joint interface but assume a stable steady-state propagation rate when reaching the fully welded overlap region. It is found that higher welding temperatures lead to longer weld lengths, which improve the strength and stiffness of the specimens and delay damage initiation. An accelerated crack growth rate indicates that the structure is close to its ultimate load after which the joint fails abruptly as the crack growth becomes unstable. Induction welding temperatures at the upper end of the recommended processing window (330 °C for T300/PPS and 385 °C for T700/LM-PAEK) result in the joints with the highest load-carrying capacity and slowest crack propagation, but also the least damage tolerance.

Keywords: thermoplastic welding; single-lap shear joint; digital image correlation; crack growth

1. Introduction

Aeronautical structures are designed to safely sustain loads at a minimum structural weight. Today, the societal desire for sustainability is another incentive for minimizing aircraft weight: greenhouse gas emissions from air travel are directly related to the amount of jet fuel burnt. However, sustainability is not only limited to weight reduction but also includes other aspects of a typical product life cycle like energy cost during production and end-of-life applications. Given these constraints, thermoplastic carbon fiber composites offer a highly desirable combination of material properties: they feature both the high strength-to-weight ratio required for lightweight structures as well as the potential for recycling. Other benefits of thermoplastics are high impact and fracture toughness, thermal stability, and chemical resistance [1].

Manufacturing aeronautical structures made from thermoplastic composites requires suitable joining methods. Several welding techniques have been developed for thermoplastic composites [2,3]. The most researched ones are induction welding, resistance welding, and ultrasonic welding [4,5]. These methods produce joints that are similar in terms of their mechanical properties [2,4]. Another promising joining technique is conduction welding

Academic Editor: Jiunn Jer Hwang

Received: 23 March 2026
Revised: 8 April 2026
Accepted: 23 April 2026
Published: 29 April 2026

because it is easily scalable for higher production volumes and larger parts [6]. Out of the four mentioned joining methods, only induction and conduction welding do not require the placement of additional material for heat generation in the weld line. This eliminates the corrosion risk of the conductive wire mesh in resistance welded joints as well as potential pore defects caused by using energy directors for ultrasonic welding [7].

Researchers have investigated induction welding since the late 1980s but mostly focused on manufacturing aspects as evidenced by the emphasis of several review papers [2,3,8–10]. Studies on the structural performance of thermoplastic welded joints were conducted by Villegas et al. [4] and Gouin et al. [5] who compared the lap shear strength of induction, resistance, and ultrasonic-welded composites. Villegas et al. [4] carried out static and fatigue tests on fabric carbon fiber/polyphenylene sulfide (CF/PPS) single-lap shear (SLS) joints. Gouin et al. [5] explored the influence of the heating rate on the joint performance. Kwon et al. [11] examined the static and fatigue strength of induction-welded SLS joints with a polyetherketoneketone (PEKK) matrix. The influence of hygrothermal effects on the static strength of CF/PEKK was investigated by Jeong et al. [12].

Publications on conduction-welded joints are more limited due to the recent development of this technique. Tijs et al. [6] tested conduction-welded unidirectional (UD) CF/PEKK SLS joints and predicted their behavior numerically. They noted that the higher-than-expected experimental results were most likely caused by a change in material properties during welding. Another contribution by Tijs et al. [13] relates the structural response of the same joints to various manufacturing parameters. Conduction welding has also been used to manufacture stiffened panels which were tested and modeled in axial compression by van Dooren and Bisagni [14].

Studies on the damage evolution in induction- and conduction-welded joints are rare. The numerical model of Tijs et al. [6] uses cohesive zone modeling (CZM) to predict the damage in the overlap area of conduction-welded joints. The second publication by Tijs et al. [13] shows that thermoplastic welding can lead to improved interface properties when compared to specimens consolidated in an autoclave process.

Damage in other types of thermoplastic welded joints was investigated by Zhao et al. [15], who implemented a rate-dependent bilinear traction–separation law for CZM to predict the damage in the weld line of resistance welded SLS joints. Sioutis et al. [16] present C-scan images of refill friction stir spot-welded thermoplastic joints at various load levels. Li et al. [17,18] correlate the electrical resistance of ultrasonic-welded SLS joints with carbon nanotubes in the weld line to damage in the structure.

Induction- and conduction-welded joints show great potential for their use in highly loaded, yet sustainable, aeronautical structures. Hence, understanding damage evolution in these joints is essential, but damage initiation and propagation can vary considerably based on the employed material constituents and processing temperatures. This paper describes an experimental campaign conducted to measure the damage evolution in induction- and conduction-welded SLS joints using digital image correlation (DIC). In this study, 24 induction-welded and 10 conduction-welded specimens, manufactured by Collins Dutch Thermoplastic Components (DTC) and the Dutch Aerospace Center (Nederlands Lucht- en Ruimtevaartcentrum, NLR) at different processing temperatures, are tested to measure their strength, stiffness, damage growth, and to investigate failure modes.

2. Welded Single-Lap Shear Joint Specimens

Two different carbon fiber-reinforced thermoplastic composites and two welding technologies are investigated experimentally. The thermoplastic composites are woven Toray Cetex® TC1100 PPS [19] and UD Toray Cetex® TC1225 LMPAEK™ [20]. Toray Cetex® TC1100 PPS consists of T300 fibers embedded in a polyphenylene sulfide matrix (T300/PPS). The

constituents of Toray Cetex® TC1225 LMPAEK™ are T700 fibers and low-melt polyaryletherketone (T700/LM-PAEK). The linear elastic material properties for both materials are summarized in Table 1.

Table 1. Lamina properties of T300/PPS [19] and T700/LM-PAEK [21].

	Unit	T300/PPS	T700/LM-PAEK
E_1	GPa	58.0	130.5
E_2	GPa	56.0	9.1
G_{12}	GPa	3.9	4.6
ν_{12}	-	n/a	0.34

The SLS specimens are joined using induction and conduction welding. Despite the various materials and welding processes, the production of all specimens follows the same general steps. First, laminates are laid up by hand for consolidation. The stacking sequence used for the woven T300/PPS laminae is $[(\pm 45)/(0/90)/(\pm 45)/\overline{(0/90)}]_S$, while $[45/90/-45/0]_{2S}$ is chosen for unidirectional T700/LM-PAEK laminae. These layups result in nominal laminate thicknesses of 2.4 mm and 2.2 mm, respectively.

Two laminates are then placed on top of each other with an overlap of 25.4 mm, along which they are welded (Figure 1). This produces a $+45°/+45°$ interface. Induction welding is carried out at the NLR and works by moving an induction coil along the weld line which induces an eddy current inside the overlap region. Here, heat is generated because of the electric resistance of the material. Once the melting temperature of the thermoplastic is reached, the polymer chains at the interface between the two laminates start to flow and entangle with each other such that they form a joint. Conduction welding is carried out at Collins DTC and follows the same procedure, but heat is transferred to the weld region via conduction from an induction-heated metal stamp that is pressed onto the overlapping laminates. In the last step of specimen production, the SLS joints are cut from the welded laminates to a width of 25.4 mm.

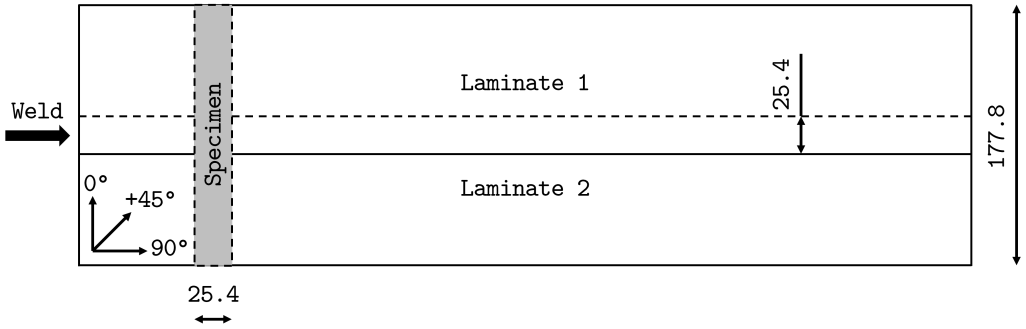

Figure 1. Welding of laminates and cutting of specimens. Dimensions in mm.

The SLS joints are welded at various temperature levels to investigate the influence of the welding temperature on the structural performance of the specimens. The target welding temperatures are the upper and lower bounds of the processing windows recommended by the material supplier (300 °C to 330 °C for T300/PPS [19] and 340 °C to 385 °C for T700/LM-PAEK [20]). Table 2 provides an overview of the seven specimen types (A–G), the number of samples available for testing, the respective thermoplastic welding processes, the welding temperatures, and the adherend materials. The listed welding temperatures are the actual temperatures measured during welding using thermocouples placed within the joints. There are three welding temperatures for the induction-welded T300/PPS specimens because the 364 °C set is additionally welded above the maximum recommended processing temperature of 330 °C. For the induction-welded T700/LM-PAEK samples, it was not

possible to reach welding temperatures significantly higher than 382 °C due to the power constraints of the welding equipment. Images of the induction- and conduction-welded specimens, as well as their corresponding IDs, are presented in Figure 2.

Table 2. Overview of SLS joints for testing.

ID	No.	Weld	Temperature	Material
A	5	Induction	364 °C	T300/PPS
B	5	Induction	338 °C	T300/PPS
C	5	Induction	315 °C	T300/PPS
D	5	Induction	382 °C	T700/LM-PAEK
E	4	Induction	340 °C	T700/LM-PAEK
F	5	Conduction	365 °C	T300/PPS
G	5	Conduction	385 °C	T700/LM-PAEK

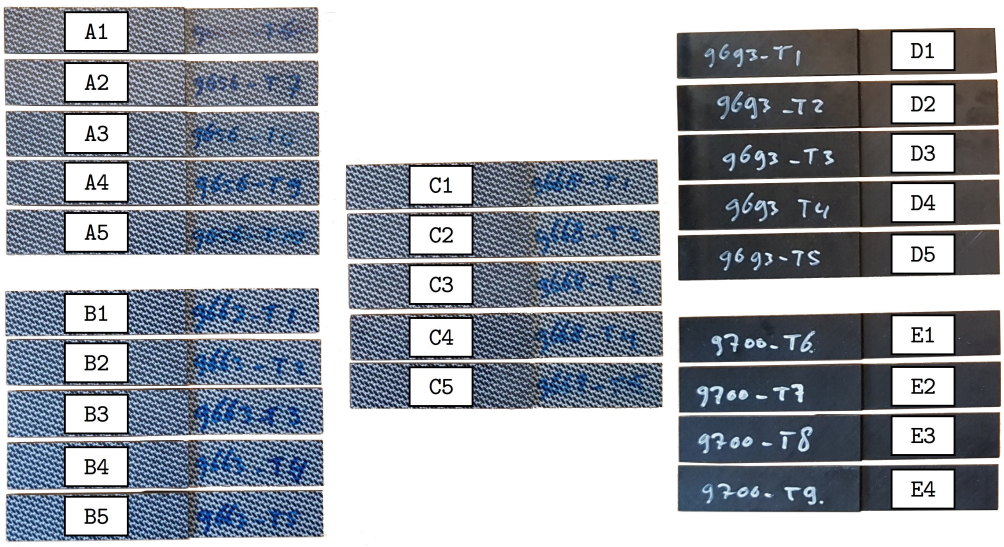

(**a**)

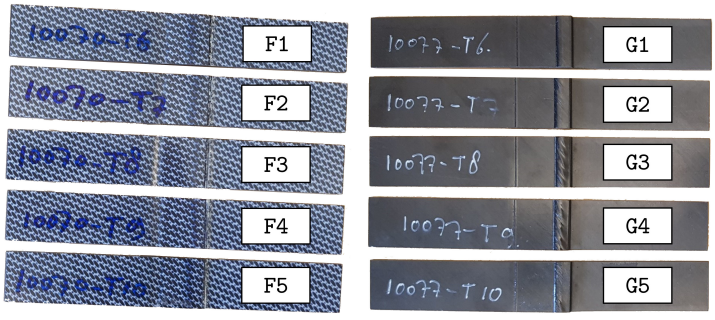

(**b**)

Figure 2. (**a**) Induction and (**b**) conduction-welded specimens.

The geometry of the SLS joints is illustrated in Figure 3. The subscripts 1, 2, and o in Table 3 refer to the three regions of the joint, i.e., adherend 1, adherend 2, and the overlap. The dimensions are those recommended by the ASTM standard D5868 [22]. Specimen preparation follows the guidelines outlined in this standard. All samples are measured before testing.

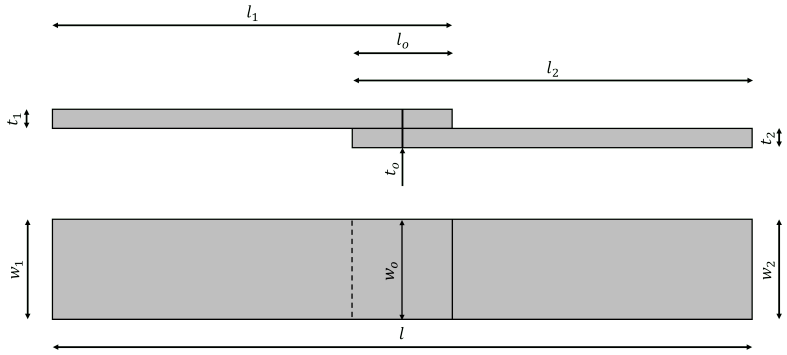

Figure 3. Sketch of the SLS joint including dimensions.

Table 3. Specimen dimensions.

	Symbol	Unit	Nominal
Total Length	l	mm	177.8
Length Adherend 1	l_1	mm	101.6
Width Adherend 1	w_1	mm	25.4
Thickness Adherend 1	t_1	mm	2.4/2.2
Length Adherend 2	l_2	mm	101.6
Width Adherend 2	w_2	mm	25.4
Thickness Adherend 2	t_2	mm	2.4/2.2
Width Overlap	w_o	mm	25.4
Thickness Overlap	t_o	mm	4.8/4.4
Length Overlap	l_o	mm	25.4

Speckle patterns for DIC are applied on the front and on the right side of the specimens. In addition, the conduction-welded SLS joints are prepared for manual crack growth measurements by cutting vertical markings with a spacing of one millimeter into the left side of the overlap region.

A photo of the induction-welded specimen A2 and of the conduction-welded specimen G3 is presented in Figure 4. Specimen G3 features a bulge at one end of the overlap region and is slightly bent. The bulge forms when the hot metal stamp applies heat and pressure to the overlap region during the welding process. Some of the thermoplastic escapes from the area underneath the stamp and reconsolidates in a less constrained region. The bending of the specimens is most likely a result of residual thermal stresses which are caused by the high processing temperatures. The joints are tested with these manufacturing imperfections.

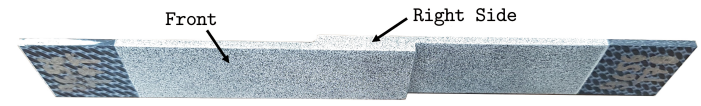

(**a**)

(**b**)

Figure 4. Images of (**a**) induction-welded specimen A2 and (**b**) conduction-welded specimen G3.

3. Experimental Methodology

The SLS joint experiments are conducted at TU Delft on a ZwickRoell machine which is shown together with the test setup in Figure 5.

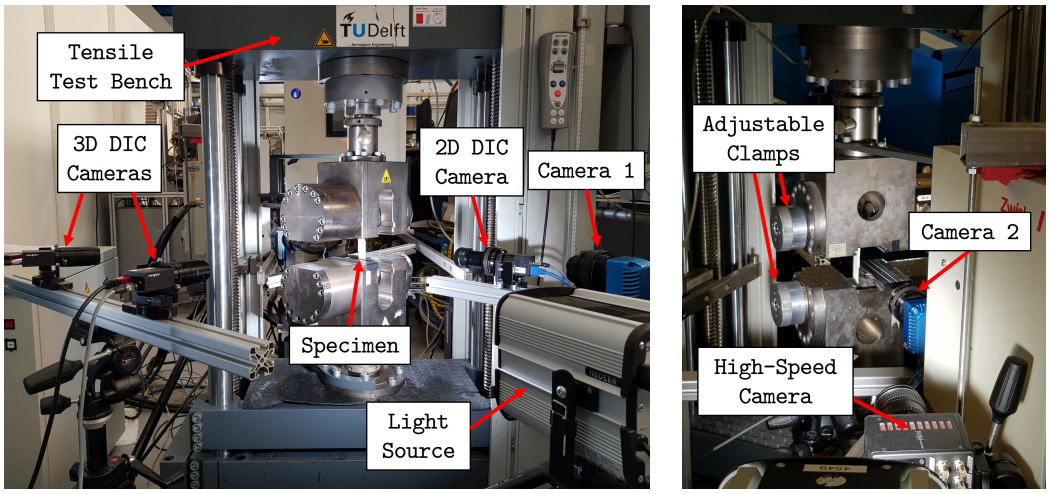

(**a**) (**b**)

Figure 5. Test setup (**a**) front view and (**b**) rear view.

During the tests, displacement and strain fields are measured on two specimen surfaces with DIC. 3D DIC is used on the frontal specimen area because of the out-of-plane deformation of the SLS joints due to secondary bending. 2D DIC is employed to track the displacement field in the overlap region on the right side of the specimens. DIC images are automatically captured at a frequency of 1 Hz with Vic-Snap 9 which is sufficient to capture the static response of the specimens.

An additional camera captures isometric images of the specimen and of the clamps. Another camera is used for the conduction-welded specimens to take pictures of the crack growth on the left side of these joints. Axial displacement loads of 0.2 mm/min for the induction-welded specimens and 0.1 mm/min for the conduction-welded joints are applied until the specimens fail. While the different loading speeds do not affect the conclusions drawn from the tests, a reduced strain rate decreases the crack propagation rate in thermoplastic polymers due to viscoplastic effects. Dynamic effects only play a significant role at higher loading speeds (>13 mm/min) [22].

For the conduction-welded specimens, a high-speed camera is employed to capture the final fracture of the specimens at 20,000 frames per second. The high-speed camera is triggered manually to save the images captured during the last three seconds of the test. After the experiments, pictures of the fracture surfaces are taken with a Keyence VR 5000 digital microscope (Keyence Corporation, Osaka, Japan).

To avoid measuring the testing machine compliance, the vertical displacement of the specimens during the tests is determined using DIC considering two points on the frontal specimen surface close to the top and bottom clamps.

Damage initiation and propagation are measured during the experiments. In composite SLS joints, damage typically materializes as cracks in the overlap region that initiate at the overlap ends and then grow towards the center of the joint [23]. 2D DIC is employed to assess the crack length in the overlap region. In particular, crack tips are detected by evaluating the strain field in the area of interest. A crack tracking algorithm is written in Python 3.6 that calls the VicPy module [24] to operate on the post-processed DIC data. If the strain at a certain position exceeds a threshold value, the corresponding location is considered to be damaged. The threshold value is taken as the strain at the crack tip in the

last DIC image before failure. Thus, crack initiation and propagation are evaluated along the joint interface starting from the two overlap ends. To overcome numerical noise caused by the DIC strain calculation, the algorithm allows cracks to "jump" over theoretically undamaged material for a short distance ahead of the current crack tip.

Since cracks reduce the stiffness of a structure, the tangent joint stiffness can also be used to quantify the damage in the joint. Assuming continuous data, the joint stiffness $k_{\tan}$ is calculated as

$$k_{\tan} = \frac{\partial F}{\partial u} \tag{1}$$

where F is the current force and u is the axial specimen displacement.

As only discrete data is available, $k_{\tan}$ is computed using a central difference scheme. The underlying data is filtered before numerical differentiation to avoid noise amplification. Two different filters are considered: a Savitzky–Golay filter of order 1 with window length 299 and a second-order low-pass Butterworth filter with a cutoff frequency of $\omega = 1.5$ Hz.

4. Results and Discussion

Here, the results from the evaluation of the test campaign are presented. First, the test results of two SLS joints are discussed in detail to showcase the structural response of woven induction-welded T300/PPS and UD conduction-welded T700/LM-PAEK SLS specimens. Then, similarities and differences between the seven specimen types in terms of strength, stiffness, damage growth, and failure modes are examined.

4.1. Induction-Welded Specimen A2

The test results for the induction-welded T300/PPS joints are discussed based on specimen A2. Figure 6 shows the corresponding load–displacement curve. The specimen is at rest at (1) and continuously loaded through (2). Cracks initiate at (3) at both overlap ends when the reaction force is approximately 5 kN. The crack propagation is stable as the displacement load increases from points (4) to (6). Small nonlinearities caused by both secondary bending and damage are observed at (7) before the ultimate load of 13.7 kN is reached. The crack growth becomes unstable and a sudden load drop is observed. The specimen fails at (8).

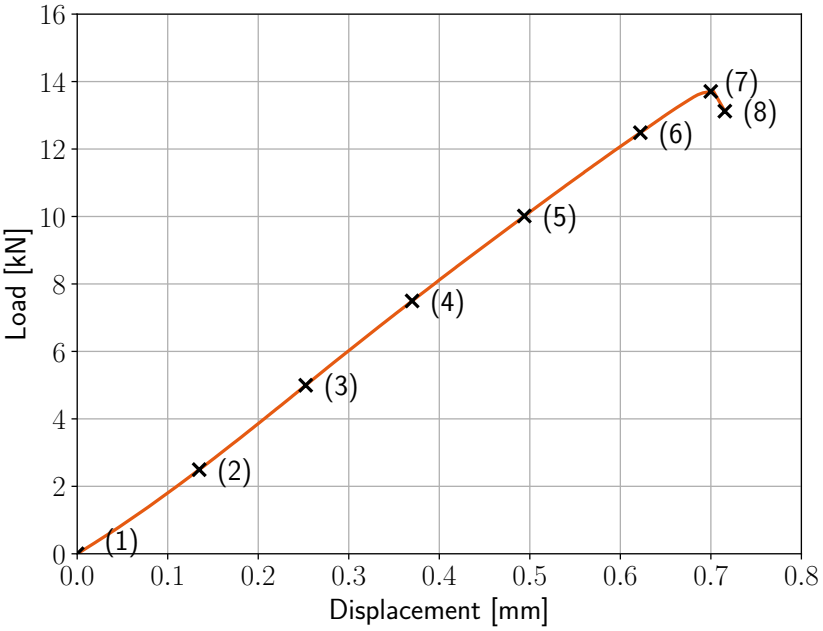

Figure 6. Load–displacement curve for specimen A2.

The tangent stiffness is evaluated to provide additional insight into the structural response of the joint. The plot of the calculated tangent stiffness versus the displacement is reported in Figure 7. It contains three different curves: No Filter uses the unfiltered load and displacement data to calculate the tangent stiffness, while Savitzky–Golay and Butterworth have the corresponding filters applied before $k_{\tan}$ is computed. The noise in the unfiltered data is amplified by the numerical differentiation. In contrast, clear trends can be inferred from the filtered tangent stiffness curves, which agree both quantitatively and qualitatively. Both filters dampen out the high-frequency response, but low-frequency signals are retained. Therefore, sudden changes in the tangent stiffness, like those caused by the load drop, are less pronounced. Since both filters provide similar results, only the Savitzky–Golay filter is taken into account in the following plots featuring the tangent joint stiffness.

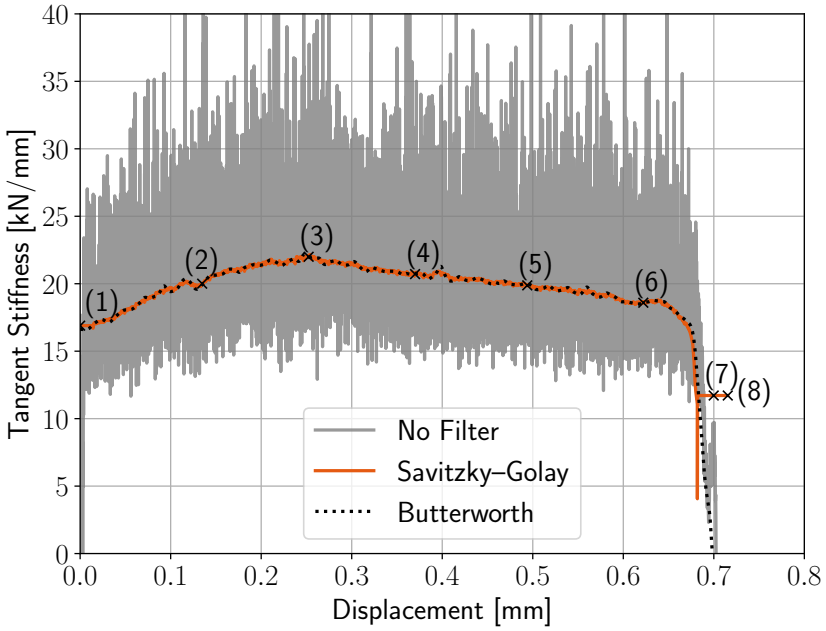

Figure 7. Tangent stiffness of specimen A2 determined from original and filtered data.

From the start of the test at (1) to (3), the tangent stiffness of the SLS specimen increases. This trend is caused by secondary bending. The overlap region aligns itself with the loading axis of the test machine and therefore the joint cross-section becomes more evenly loaded. Hence, the effective joint stiffness increases. After (3), the tangent stiffness starts to decrease at a constant rate as cracks initiate at both overlap ends. The constant reduction in stiffness is associated with stable crack growth in the overlap area. As the stiffness increase due to secondary bending and the stiffness decrease because of crack growth occur simultaneously, the tangent stiffness reduction through (4) and (5) must be interpreted as the delta between these two effects. After (6), the tangent stiffness decreases rapidly which indicates that the maximum load is being approached. For (7) and (8), the structural response is increasingly influenced by high-frequency effects, and the filtered data ceases to provide meaningful information.

Damage in the form of cracks is visualized in Figure 8, where the strain contours are plotted. While only the major principal strain ε_1 is presented here, similar plots can also be generated for other strain measures. The advantage of using a principal strain is its independence from the reference frame, i.e., neither curved specimen features nor any in-plane rotation of the DIC camera affect the results.

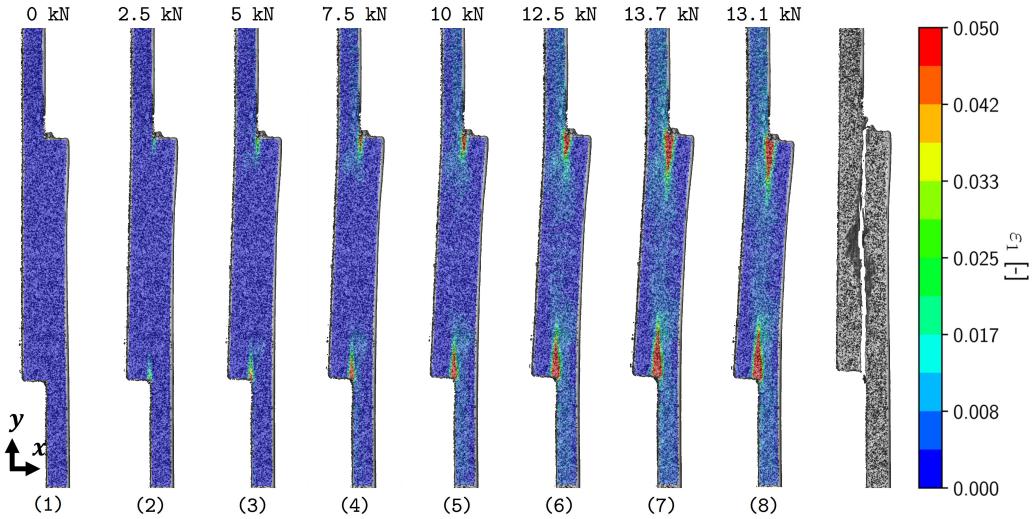

Figure 8. Principal strain ε_1 distribution during loading of specimen A2.

The reference image of the clamped, but undeformed, structure with zero strain is shown in (1). Secondary bending is observed at loads as low as 2.5 kN (2), where strain concentrations are already visible. When taking the strain value at the crack tip in the last image before failure (5%) as the threshold value, crack initiation may be recognized at the overlap ends in (3). The overlap region continues to bend in the following images. Furthermore, the strain concentrations at the top and bottom overlap ends extend towards the center of the overlap in pictures (4)–(6). The maximum load is reached in (7) and a last picture (8) is taken before the specimen fails. From image (7) to (8), the strain field extrema move noticeably towards the center of the overlap in one frame. The last picture shows the specimen after failure. The energy released during failure is large enough to damage the speckle pattern. Crack propagation occurs exclusively along the weld line.

The fracture surfaces of specimen A2 are shown in Figure 9. While the overlap region is welded in its center, the overlap ends remain unwelded. The weld length is practically constant along the overlap width. Some fiber pull-out and the $+45°/+45°$ interface are visible. It is also possible to note that polymer-rich regions, which probably formed during welding, are more pronounced towards the boundary between the welded and unwelded parts of the interface. They are complemented by fiber-rich regions on the respective opposing fracture surfaces. Furthermore, polymer discoloration can be seen, which indicates an exposure to higher temperatures, as the induction coil was moved along this adherend.

4.2. Conduction-Welded Specimen G3

The test results for the conduction-welded T700/LM-PAEK SLS joints are discussed based on specimen G3. The load–displacement curve is shown in Figure 10. In addition, the strain field measured by DIC on the right side of the specimen and the crack growth images taken by the second camera on the left specimen surface are reported in Figure 11. These images correspond to the labeled points on the load–displacement curve.

Point (1) marks the start of the test. Significant strain concentrations are visible at the overlap ends for a load of 1.6 kN at (2). Two cracks can be seen at (3) in the DIC pictures, but damage at both overlap ends is only visible in the crack growth images in (4). The cracks propagate along the weld line in (5) and (6) as the joint aligns itself with the test machine. The maximum load of the specimen is reached in (7) at 11.4 kN. Considerable crack growth can be observed from (7) to (8) in only 5 frames. The last image shows the specimen after failure.

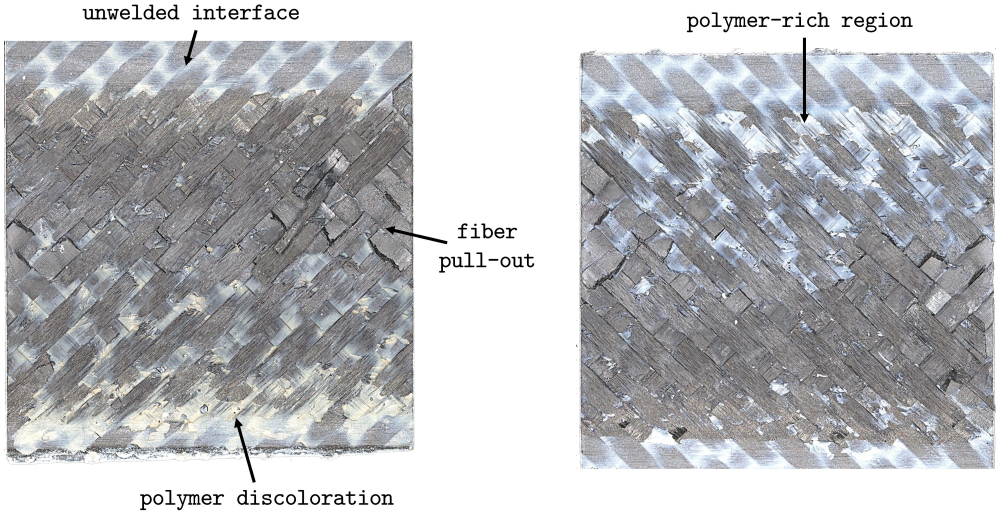

Figure 9. Fracture surfaces of specimen A2 on the (**a**) top and (**b**) bottom adherend.

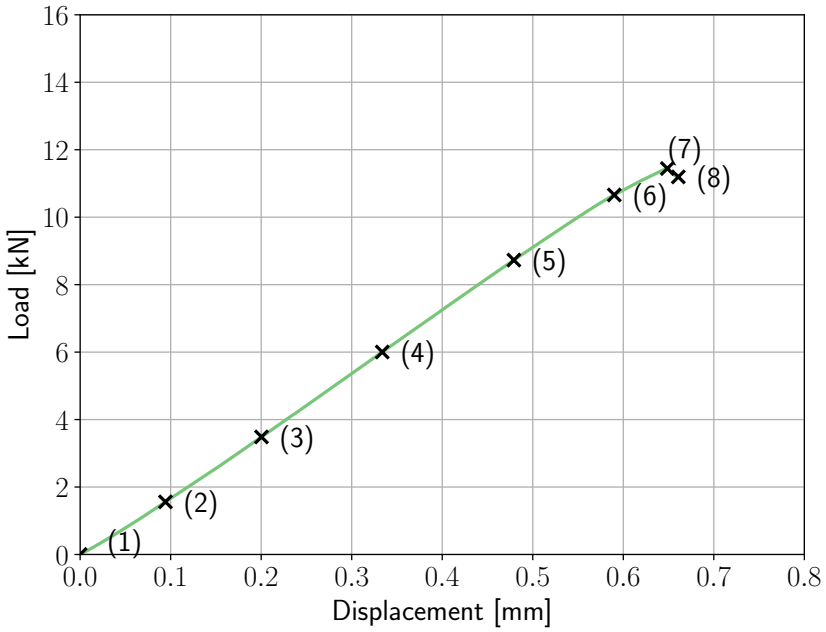

Figure 10. Load–displacement curve for specimen G3.

The crack length measured using DIC in Figure 11a and the crack length taken from the images in Figure 11b are compared as a function of the applied displacement load. Again, the strain value at the crack tip location in the last image before specimen failure is considered as the threshold value for damage in the overlap region, and is rounded to 5%. Additionally, the upper and lower crack measurement bounds are computed assuming threshold values of 4% and 6%, which are plotted in Figure 12a as shaded regions to demonstrate the robustness of the procedure irrespective of the exact threshold value. A similar image-based crack length measurement technique is validated in [25].

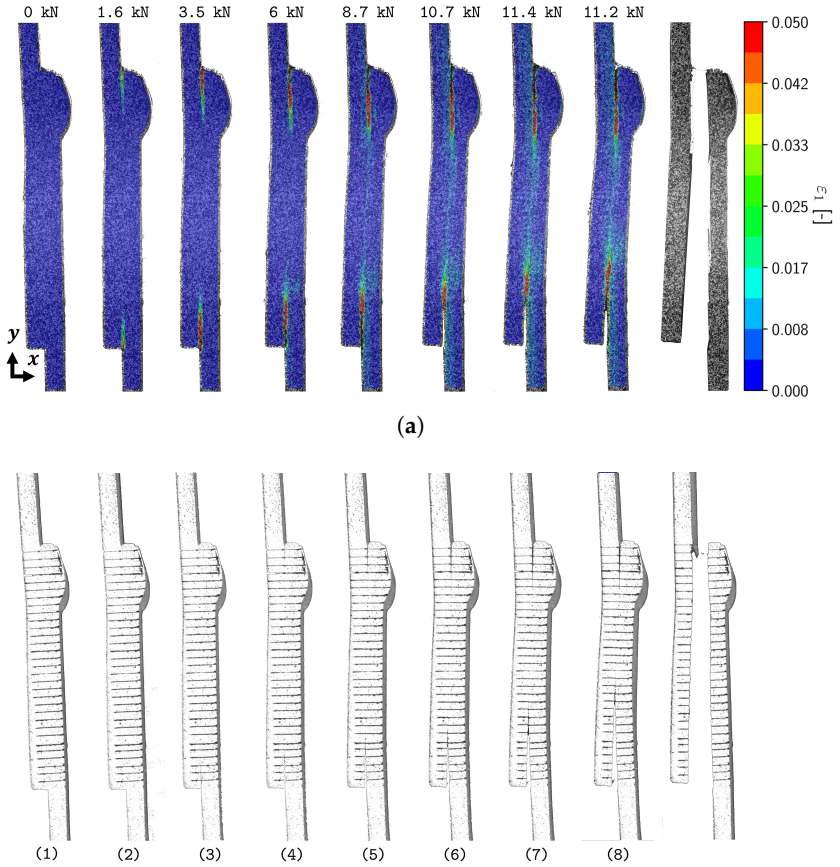

Figure 11. Damage in specimen G3 visualized using (**a**) principal strain measured by DIC and (**b**) crack growth images.

According to the crack measurement using markings, damage at the bottom overlap end is only clearly visible at (3) for a load of 3.5 kN. Damage initiation at the top overlap end is observed later at 6 kN (4). Furthermore, the crack at the bottom overlap propagates to a length of 13 mm at failure compared to a 6 mm long crack at the top overlap end.

While the manual and DIC crack growth measurement techniques agree reasonably well at the bottom overlap end, they do not at the top overlap end. One reason for this is that the two cameras are pointed at opposite sides of the specimen. Since off-angle ply interfaces cause an asymmetric crack front shape over the specimen width, this can lead to different crack lengths on each side. In any case, the DIC approach enables a more precise tracking of the crack tip due to the higher number of data points.

Three distinct crack growth phases are observed in specimen G3, as shown in Figure 12a. After damage initiation, crack growth is relatively fast. Next, the crack growth rate slows down and becomes constant. Both phases are characterized by stable crack growth since the specimen is able to carry additional loads despite damage accumulation. Close to the ultimate load, the crack growth accelerates and becomes unstable which leads to the failure of the joint.

These three phase are also clearly visible in Figure 12b, where the total crack length in the overlap region is plotted together with the tangent stiffness of the joint. Damage initiation correlates with the stiffness drop at (2). The joint stiffness remains relatively constant in the second damage growth phase from (3) to (5). Then, the rapid crack growth phase occurs together with the joint stiffness reduction from (5) to (6).

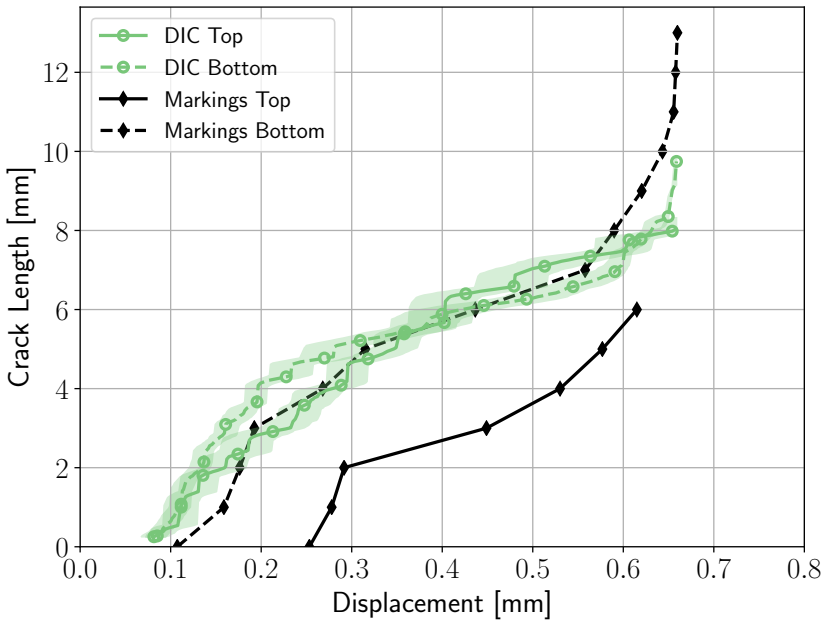

(**a**)

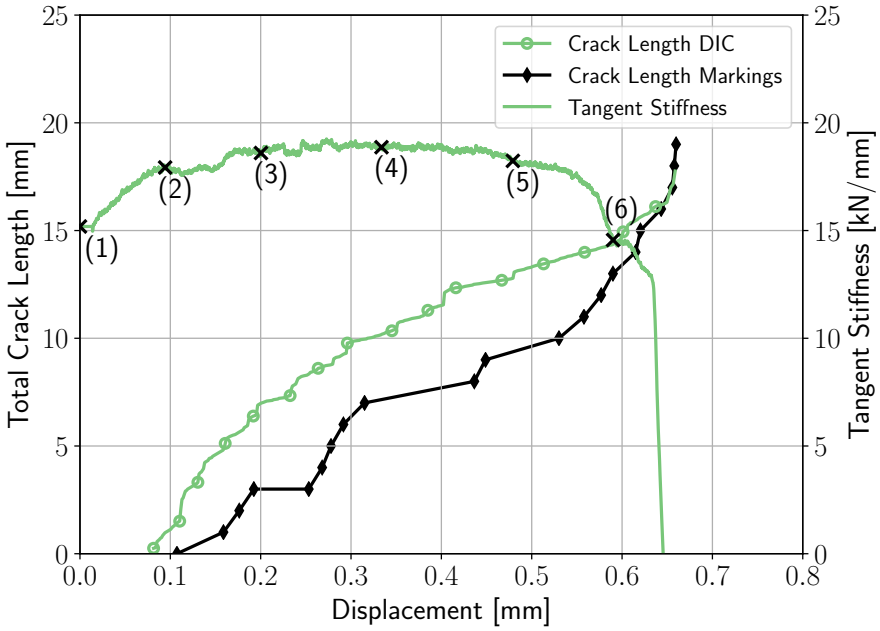

(**b**)

Figure 12. Crack length measurements (**a**) at both overlap ends with the shaded region highlighting the DIC measurement uncertainty and (**b**) correlated to the tangent joint stiffness.

The fracture surfaces of specimen G3 are shown in Figure 13. A clear distinction can be made between the welded and the unwelded parts of the interface, including a transition region separating the two. The partial delamination of the 90° plies underneath the +45°/+45° interface indicates high interlaminar stresses between the 45° and the 90° plies and a potential variation in interlaminar properties across the overlap width. Additionally, the slanted weld line across the joint width contributes to the difference in crack length measurements between the manual and the DIC approaches at the top overlap end in Figure 12a.

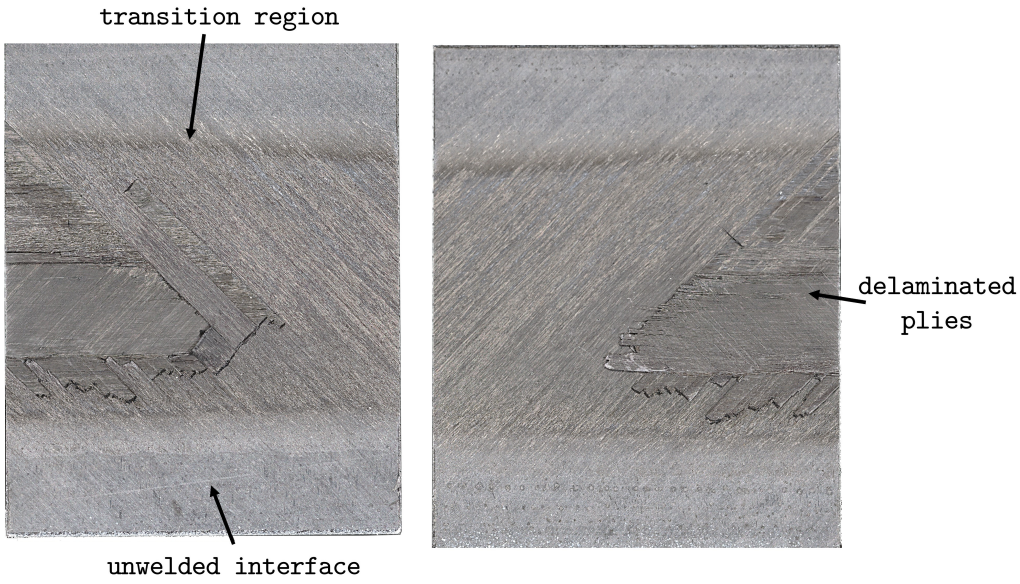

Figure 13. Fracture surfaces of specimen G3 on the (**a**) top and (**b**) bottom adherend.

4.3. Comparison of the Seven Specimen Types

An overview of the load-carrying capacity of the seven specimen types is given in Table 4 which contains the respective maximum load (F_{max}) and apparent shear strength (τ_{max}) values. Arithmetic means and standard deviations are reported. The shear strength is calculated as

$$\tau_{max} = \frac{F_{max}}{w_o l_o} \quad (2)$$

where w_o and l_o are the dimensions illustrated in Figure 3, measured for each specimen.

Table 4. Average test results for each specimen type, including standard deviations.

ID	Weld	Temperature	Material	F_{max} [kN]	τ_{max} [MPa]
A	Induction	364 °C	T300/PPS	13.42 ± 0.31	20.40 ± 0.51
B	Induction	338 °C	T300/PPS	10.74 ± 0.11	16.47 ± 0.19
C	Induction	315 °C	T300/PPS	9.98 ± 0.08	15.07 ± 0.11
D	Induction	382 °C	T700/LM-PAEK	14.86 ± 1.11	22.58 ± 1.62
E	Induction	340 °C	T700/LM-PAEK	9.73 ± 0.41	14.88 ± 0.64
F	Conduction	365 °C	T300/PPS	13.89 ± 1.56	15.79 ± 1.56
G	Conduction	385 °C	T700/LM-PAEK	10.98 ± 1.58	13.32 ± 1.84

The induction-welded T300/PPS samples feature low standard deviations, which indicates a consistent manufacturing process. The higher standard variations in group D are caused by a single outlier (specimen D1) which failed at a 16% lower load than the remaining samples in the set and also featured a different failure mode. A clear trend towards higher maximum loads and shear strengths with increasing welding temperature is visible in the sets {A,B,C} and {D,E}.

The joint strength of the conduction-welded specimen types F and G, reported in Table 4, is influenced by the manufacturing imperfections observed in these samples which reduce the apparent shear strength compared to the more pristine induction-welded joints. Additionally, the strength of the conduction-welded samples F and G correlates with their position during welding. This suggests an uneven temperature distribution along the weld line which further reduces the joint strength and causes the larger scatter in the test results.

A comparison of the measured apparent shear strengths with values from the literature is provided in Table 5. The references calculate the apparent shear strength as

$$\tau_{\mathrm{max,weld}} = \frac{F_{\mathrm{max}}}{A_{\mathrm{weld}}} \tag{3}$$

where A_{weld} is the actual welded interface area.

Table 5. Comparison of the measured apparent shear strengths with values from the literature.

Reference	Material	Weld	$\tau_{\mathrm{max,weld}}$ [MPa]	Standard Deviation [MPa]
This work, type A	T300/PPS	Induction	25.9	1.4
This work, type B	T300/PPS	Induction	28.2	1.6
This work, type C	T300/PPS	Induction	29.0	0.5
This work, type D	T700/LM-PAEK	Induction	28.4	1.8
This work, type E	T700/LM-PAEK	Induction	29.6	0.3
Villegas et al. [4]	CF/PPS	Induction	27.3	0.4
O'Shaughnessey et al. [5]	AS4/PPS	Induction	31.3	3.5
Kwon et al. [11]	CF/PEKK	Induction	33.2	-
Jeong et al. [12]	CF/PEKK	Induction	31.2	1.8
This work, type F	T300/PPS	Conduction	27.4	3.1
This work, type G	T700/LM-PAEK	Conduction	20.7	3.0
Tijs et al. [6]	AS4D/PEKK	Conduction	41.7	5.3

While the apparent shear strengths for the induction-welded joints are comparable, the conduction-welded specimens perform significantly worse than the reference joints from the literature. This drop-off is probably caused by the aforementioned manufacturing imperfections.

Furthermore, the use of Equation (3) instead of Equation (2) causes the apparent shear strength to increase with decreasing welding temperatures. This trend inversion is discussed later in the context of the fracture surface evaluation.

Representative load–displacement curves for each specimen set are plotted in Figure 14. A2, B3, and C4 are selected for induction-welded woven T300/PPS SLS joints, D2 and E3 for induction-welded UD T700/LM-PAEK SLS joints, as well as F4 and G3 for conduction-welded woven T300/PPS and UD T700/LM-PAEK SLS joints. The graph shows that higher welding temperatures not only lead to an increased maximum load, but also to a stiffer structural response.

The structural behavior discussed for specimens A2 and G3 holds for all other specimens with the exception of type F. These specimens feature damage and failure modes that are not typical for SLS joints and are therefore not investigated further. The crack growth from the bottom overlap end towards the weld interface, as shown in Figure 15a occurs suddenly and causes the stiffness drop at a displacement of 0.4 mm, shown in Figure 14. The fracture surface of the specimen in Figure 15b is characterized by a curved weld interface. Still, all specimens exhibit an initial stiffening and subsequent softening, and fail abruptly after the ultimate load is reached. This highlights the need for a robust assessment of the damage accumulation in SLS joints.

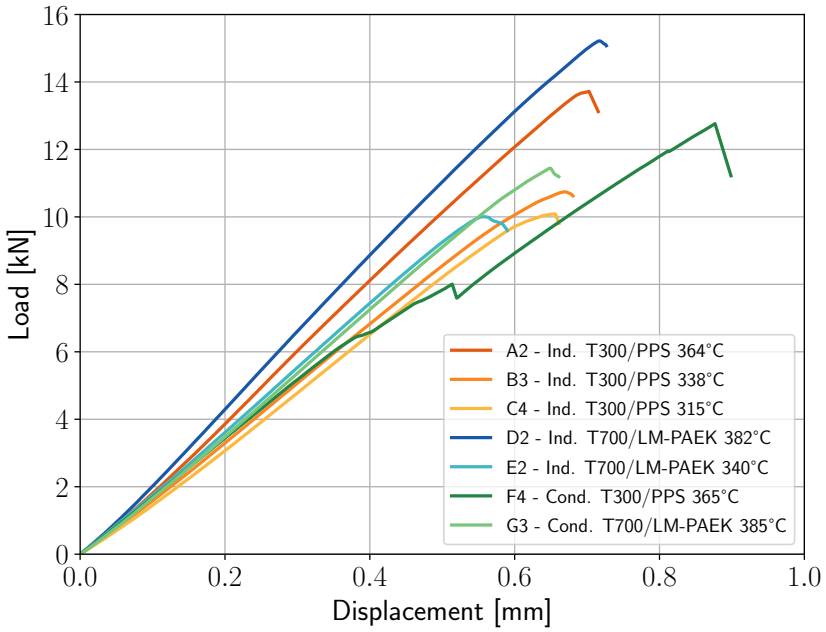

Figure 14. Load–displacement curves for all specimen sets.

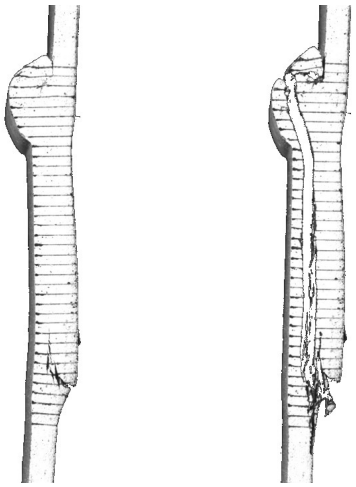

(**a**) (**b**)

Figure 15. Specimen F4: (**a**) crack propagation and (**b**) failure.

Comparing the DIC crack growth measurements in Figure 16a, considering a strain threshold value of 5% for the presence of damage in all specimens, and relating them to the corresponding tangent joint stiffnesses in Figure 16b leads to several observations. It is noted, however, that the crack propagation rate in the conduction-welded joint G3 is artificially decreased compared to the induction-welded specimens because of the lower loading speed (0.1 mm/min for the conduction-welded specimens compared to 0.2 mm/min for the induction-welded joints). Due to the viscoplasticity observed in thermoplastics, this leads to a larger fracture process zone ahead of the crack tip in the conduction-welded joint which reduces the crack propagation rate.

Nevertheless, damage initiates and propagates relatively symmetrically in specimens B3, C3, E2, and G3. Less symmetric damage growth is observed for samples A2 and D2, which are welded at higher temperatures.

Furthermore, there are distinct crack growth patterns in specimens welded at lower temperatures (B,C,E) compared to samples welded at higher temperatures (A,D). For lower welding temperatures, damage initiates earlier and propagates relatively quickly until

a steady-state crack growth rate is reached. Once the ultimate load of the structure is approached, the crack growth accelerates again.

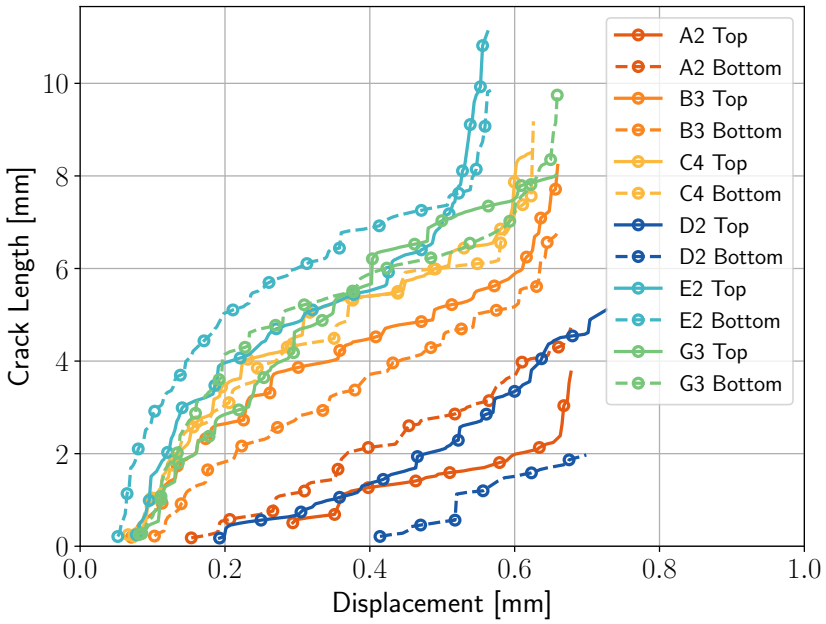

(**a**)

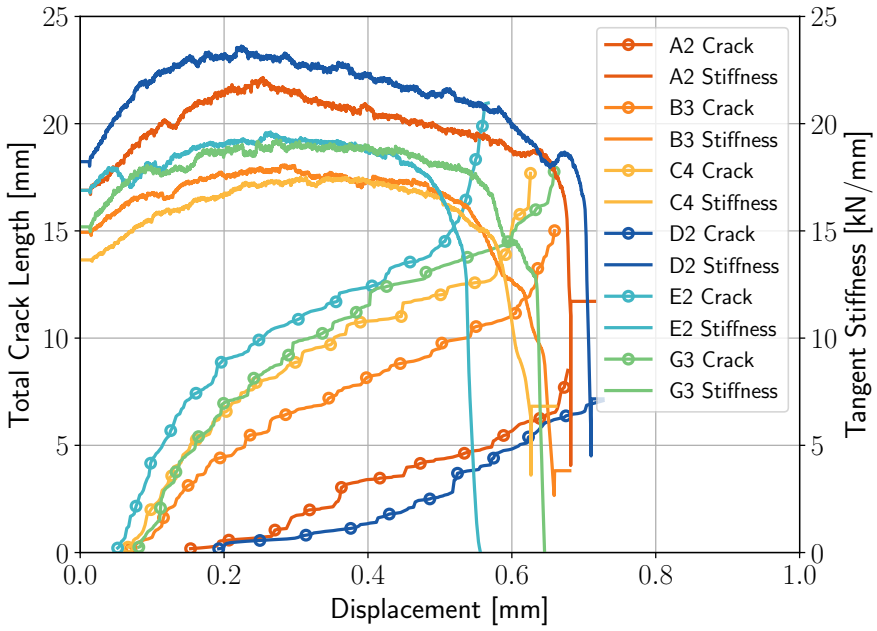

(**b**)

Figure 16. Crack length measurements (**a**) at both overlap ends and (**b**) the total crack length correlated to the tangent joint stiffness for different specimen sets.

Conversely, for higher welding temperatures, damage initiation occurs later. In addition, crack growth rates are lower. Specimens welded at higher temperatures do not feature a rapid initial crack growth rate but appear to immediately experience a steady-state response. The fact that this steady-state crack growth rate decreases with increasing welding temperature suggests that higher welding temperatures have a positive effect on the fracture toughness of the material. In any case, faster damage propagation close to the maximum load is also observed for these specimens.

Another consequence of the varying crack growth rates is that joints welded at lower temperatures feature longer cracks at failure, whereas specimens welded at higher temperatures reach the ultimate load level when the total crack length is still relatively short. A welding temperature of 338 °C is considered as reasonable trade-off between static strength and static damage tolerance for the induction-welded T300/PPS joints. If the minimum detectable crack length is 4 mm, then a welding temperature of 364 °C leads to crack lengths at failure that do not permit an appropriate level of damage tolerance. For the same reason, a welding temperature of 340 °C is preferred for the induction-welded T700/LM-PAEK joints.

Figure 16b shows that all samples feature stable crack growth as damage accumulates slowly while the SLS joints take on additional load. The maximum tangent joint stiffness is reached once the softening effect of the crack propagation exceeds the stiffening effect of secondary bending. It is evident that both a significant decrease in the tangent joint stiffness and a rapid increase in crack growth rate indicate a load level that is close to the ultimate load of the joint.

Figure 17 presents images of the fracture surfaces of induction-welded joints taken after the tests. Welded and unwelded regions can be clearly distinguished. The T300/PPS joints (type A, B, and C) feature a constant weld length across the overlap width, whereas the T700/LM-PAEK joints (type D and E) show a bias towards one side of the overlap region. Furthermore, it is obvious that higher welding temperatures lead to longer weld lengths.

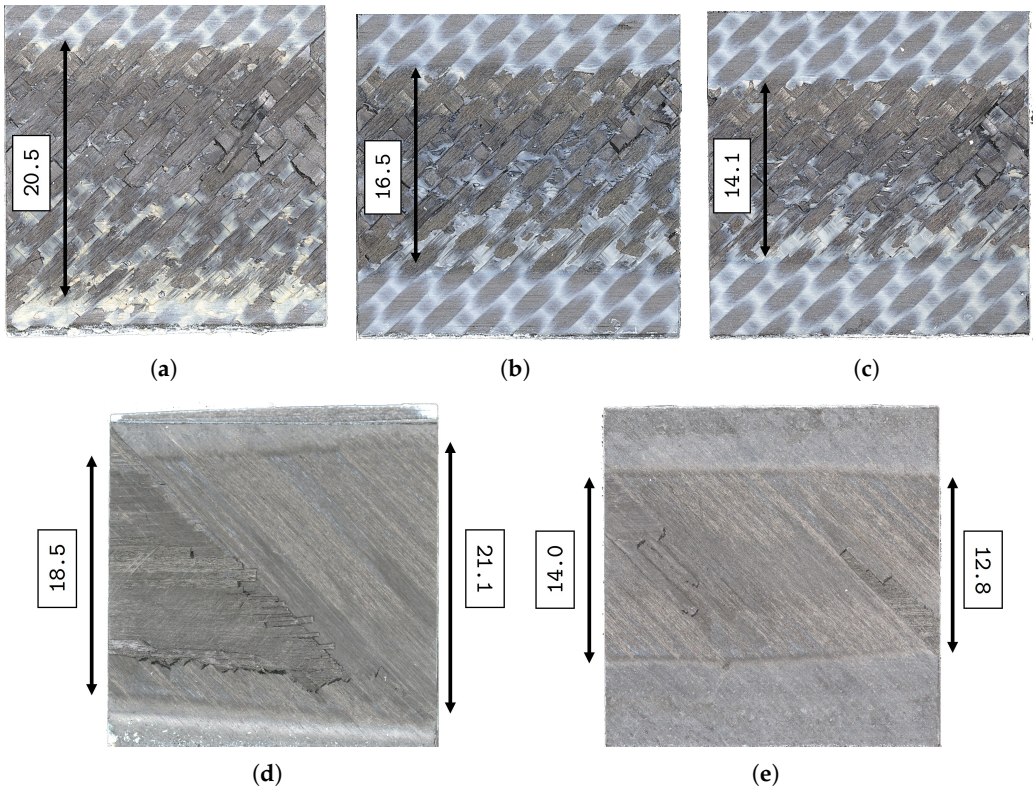

Figure 17. Fracture surfaces of specimens (**a**) A2, (**b**) B3, (**c**) C4, (**d**) D1, and (**e**) E2.

The influence of the welding temperature on the crack growth rates shown in Figure 16 is the result of two physical changes in the overlap regions. Firstly, the welding temperature affects the fracture toughness properties in the weld line [13]. Secondly, higher welding temperatures lead to longer welds which means that the unwelded regions at the overlap ends are shorter. Hence, higher welding temperatures lead to joints with tougher material closer to the overlap ends that resist crack growth sooner and more effectively. As a

result, there is less total crack growth in the specimens welded at higher temperatures before failure.

Longer weld lengths caused by higher welding temperatures provide a physical explanation for the trends observed in Figure 14. A larger weld area enables the joint to carry higher loads because more material is used. Therefore, it also increases both the maximum load of the joint as well as its stiffness.

The influence of the welding temperature on the apparent shear strength depends on the area used for normalizing the maximum load, as demonstrated by the results of Equations (2) and (3) in Tables 4 and 5. Since the apparent shear strength is a design value, it is a function of the material properties and the joint geometry. To separate these effects, the influence of the adherend thickness t and of the weld length $2c$ on the joint performance is approximated using analytical equations.

First, the influence of these parameters on the bending moment at the joint ends due to the eccentricity of the load path is investigated. Hart-Smith [26] derived the equation

$$M_O = P\frac{t}{2\left(1+\xi c+\frac{\xi^2 c^2}{6}\right)} \tag{4}$$

which relates the bending moment per unit width at one overlap end M_O to the axial force per unit width P with $\xi = \sqrt{P/D}$, where D is the bending stiffness of one of the adherends. Equation (4) is evaluated using the material properties of T700/LM-PAEK for different values of c and t. P is kept constant at 10 N/mm, which is representative of a load level that a joint experiences at the start of a test. The corresponding results are presented in Table 6.

Table 6. Influence of the adherend thickness t and half the weld length c on the bending moment at one overlap end M_O for an axial load of $P = 10$ N/mm.

t [mm]	c [mm]	c/t [-]	M_O [Nmm/mm]
1	5	5	4.00
1	10	10	3.29
1	15	15	2.76
2	5	2.5	9.20
2	10	5	8.51
2	15	7.5	7.90
4	5	1.25	19.41
4	10	2.5	18.85
4	15	3.75	18.32

It is evident that shorter overlap lengths lead to more secondary bending which decreases the joint efficiency. Therefore, joints with longer weld lengths, i.e., those welded at higher temperatures, are more efficient at minimizing the peel stresses at the overlap ends. Even though thicker adherends cause higher bending moments M_O, the corresponding peel stresses are smaller than those in thinner adherends because of the disproportional increase in the second moment of area which resists the bending deformation.

The same ratio of c/t can lead to different values of M_O, as shown for the case of $c/t = 5$. This is due to the fact that the bending stiffness D scales cubically with the adherend thickness t in ξ in Equation (4). The ratio M_O/P decreases as P increases because the overlap region bends into the load path which reduces the eccentricity that leads to the bending moment M_O. For example, if $t = 2$ mm and $c = 10$ mm, then the ratio M_O/P is equal to 0.63 Nmm/N for $P = 100$ N/mm, but it reduces to $M_O/P = 0.44$ Nmm/N for $P = 400$ N/mm.

Another formula derived by Hart-Smith [26], namely his Equation (40), relates the average shear stress in the joint to the peak shear stress along the interface length. This equation is used to evaluate the effect of the weld length on the apparent shear strength. While the equation assumes a microscopically distinct region in the weld interface as well as a linear elastic material response, both of which are not true for the thermoplastic welded joints, it nevertheless provides some qualitatively useful information. The outputs of the equation are reported in Table 7 for the induction-welded joints at their maximum load.

Table 7. Influence of the actual weld length on the shear stress transfer efficiency $\tau_{max,weld}/\tau_{peak}$.

ID	Actual Weld Length $2c$ [mm]	Maximum Load F_{max} [kN]	$\tau_{max,weld}$ [MPa]	$\tau_{max,weld}/\tau_{peak}$ [%]
A	20.5	13.4	25.9	8.7
B	15.1	10.7	28.2	10.4
C	13.6	10.0	29.0	11.0
D	10.6	14.9	28.4	9.0
E	13.0	9.7	29.6	11.4

Table 7 shows that shorter weld lengths increase the shear stress transfer efficiency across the weld interface. This happens because the center part of the welded overlap region becomes more highly loaded the shorter the actual weld length is. However, the peak stresses at the overlap ends are more relevant for the true joint shear strength. For joint type B to reach the same peak stress as joint type A, it would need to transfer a maximum load of around 11.9 kN instead of 10.7 kN, according to the analysis. If joint B had the same shear stress transfer efficiency as joint A, its maximum load would amount to 9.0 kN instead of 10.7 kN. Similar results are obtained when other joint IDs are compared.

In summary, shorter reference weld lengths can result in a misleading increase in the apparent joint shear strength, which does not accurately represent the true shear strength of the joint. Furthermore, longer weld lengths lead to reduced bending moments at the overlap ends and therefore to lower peel stresses, which are known to be critical from an overall joint strength perspective. Therefore, it is concluded that the shear strengths reported in Table 4 (force per unit nominal weld area) are more representative of the true joint strength than the shear strengths presented in Table 5 (force per unit actual weld area).

5. Conclusions

This study investigated the influence of the welding temperature on the damage initiation and propagation in thermoplastic welded single-lap shear joints. Woven T300/polyphenylene sulfide (T300/PPS) and unidirectional T700/low-melt polyaryletherketone (T700/LM-PAEK) composite single-lap shear joints were induction- and conduction-welded and tested experimentally. The displacement and strain fields on the side and front of the specimens were measured with 2D and 3D digital image correlation (DIC), respectively. Damage in the form of cracks was tracked by evaluating the DIC strain fields. Crack growth is observed to be stable until the maximum load is reached. Failure is anticipated by a rapid increase in crack growth rate as well as a sudden drop in tangent joint stiffness. It is found that the welding temperature has a significant influence on the strength, stiffness, damage evolution, and failure mode of the joints. A higher welding temperature leads to longer weld lengths which increases both joint strength and stiffness. In addition, it delays the damage initiation and results in shorter total crack lengths at ultimate load. In contrast, lower welding temperatures provide a higher level of damage tolerance. This study contributes new insights into the quantification and evolution of damage in thermoplastic welded joints. It also demonstrates that induction-welded T300/PPS and T700/LM-PAEK

joints can be suitable for aerospace applications because of their consistent test results and damage tolerance characteristics.

Author Contributions: Conceptualization, A.S. and C.B.; methodology, A.S. and C.B.; software, A.S.; validation, A.S.; formal analysis, A.S.; investigation, A.S.; data curation, A.S.; writing—original draft preparation, A.S.; writing—review and editing, A.S. and C.B.; visualization, A.S.; supervision, C.B.; funding acquisition, C.B. All authors have read and agreed to the published version of the manuscript.

Funding: This research was funded by the European Union's Horizon 2020 research and innovation program under grant agreement number 101006952.

Data Availability Statement: The original data presented in the study are openly available in the Zenodo repository at https://doi.org/10.5281/zenodo.18519928.

Acknowledgments: The authors thank Collins DTC and the NLR for specimen production.

Conflicts of Interest: The authors declare no conflicts of interest.

References

1. Tijs, B.; Abdel-Monsef, S.; Renart, J.; Turon, A.; Bisagni, C. Characterization and analysis of the interlaminar behavior of thermoplastic composites considering fiber bridging and R-curve effects. *Compos. Part A Appl. Sci. Manuf.* **2022**, *162*, 107101. https://doi.org/10.1016/j.compositesa.2022.107101.
2. Ageorges, C.; Ye, L.; Hou, M. Advances in fusion bonding techniques for joining thermoplastic matrix composites: A review. *Compos. Part A Appl. Sci. Manuf.* **2001**, *32*, 839–857. https://doi.org/10.1016/S1359-835X(00)00166-4.
3. Reis, J.; de Moura, M.; Samborski, S. Thermoplastic composites and their promising applications in joining and repair composites structures: A review. *Materials* **2020**, *13*, 5832. https://doi.org/10.3390/ma13245832.
4. Villegas, I.; Moser, L.; Yousefpour, A.; Mitschang, P.; Bersee, H. Process and performance evaluation of ultrasonic, induction and resistance welding of advanced thermoplastic composites. *J. Thermoplast. Compos. Mater.* **2013**, *26*, 1007–1024. https://doi.org/10.1177/0892705712456031.
5. O'Shaughnessey, P.G.; Dubé, M.; Villegas, I. Modeling and experimental investigation of induction welding of thermoplastic composites and comparison with other welding processes. *J. Compos. Mater.* **2016**, *50*, 2895–2910. https://doi.org/10.1177/0021998315614991.
6. Tijs, B.; Doldersum, M.; Turon, A.; Waleson, J.; Bisagni, C. Experimental and numerical evaluation of conduction welded thermoplastic composite joints. *Compos. Struct.* **2022**, *281*, 114964. https://doi.org/10.1016/j.compstruct.2021.114964.
7. Wang, X.; Quan, D.; Liu, J.; Yue, D.; Pan, J.; Zhao, G. Towards ultrasonic welding of robust thermoplastic composite joints without the use of energy directors. *Compos. Part B Eng.* **2025**, *302*, 112561. https://doi.org/10.1016/j.compositesb.2025.112561.
8. Ahmed, T.; Stavrov, D.; Bersee, H.; Beukers, A. Induction welding of thermoplastic composites—An overview. *Compos. Part A Appl. Sci. Manuf.* **2006**, *37*, 1638–1651. https://doi.org/10.1016/j.compositesa.2005.10.009.
9. Bayerl, T.; Duhovic, M.; Mitschang, P.; Bhattacharyya, D. The heating of polymer composites by electromagnetic induction—A review. *Compos. Part A Appl. Sci. Manuf.* **2014**, *57*, 27–40. https://doi.org/10.1016/j.compositesa.2013.10.024.
10. Choudhury, M.; Debnath, K. A review of the research and advances in electromagnetic joining of fiber-reinforced thermoplastic composites. *Polym. Eng. Sci.* **2019**, *59*, 1965–1985. https://doi.org/10.1002/pen.25207.
11. Kwon, B.; Choe, H.; Jeong, J.; Ju, H.; Kweon, J.; Nam, Y. Static and fatigue behavior of induction-welded single lap carbon fiber reinforced polyetherketoneketone thermoplastic composite joints. *J. Compos. Mater.* **2021**, *55*, 4183–4193. https://doi.org/10.1177/00219983211033891.
12. Jeong, J.; Lee, D.; Ju, H.; Kweon, J.; Nam, Y. Effect of hygrothermal condition on single-lab shear behavior of induction-welded CF/PEKK thermoplastic composites. *Adv. Compos. Mater.* **2023**, *32*, 657–673. https://doi.org/10.1080/09243046.2022.2128267.
13. Tijs, B.; Turon, A.; Bisagni, C. Characterization and analysis of conduction welded thermoplastic composite joints considering the influence of manufacturing. *Compos. Struct.* **2024**, *348*, 118505. https://doi.org/10.1016/j.compstruct.2024.118505.
14. van Dooren, K.; Bisagni, C. Design, analysis and testing of thermoplastic welded stiffened panels to investigate skin-stringer separation in post-buckling. *Compos. Part B Eng.* **2023**, *267*, 111033. https://doi.org/10.1016/j.compositesb.2023.111033.
15. Zhao, G.; Xu, J.; Fan, X.; Jian, X.; Zhang, S.; Xu, J. Rate-dependent properties of resistance-welded carbon fiber-reinforced polyetheretherketone joints: Simulations and experiments. *Eng. Fract. Mech.* **2023**, *284*, 109179. https://doi.org/10.1016/j.engfracmech.2023.109179.

16. Sioutis, I.; Tserpes, K.; Tsiangou, E.; Boutin, H.; Allègre, F.; Blaga, L. Experimental evaluation of Refill Friction Stir Spot Welds (RFSSW) as crack arrest features in co-consolidated thermoplastic laminates. *Compos. Struct.* **2023**, *309*, 116754. https://doi.org/10.1016/j.compstruct.2023.116754.
17. Li, W.; Frederick, H.; Palardy, G. Multifunctional films for thermoplastic composite joints: Ultrasonic welding and damage detection under tension loading. *Compos. Part A Appl. Sci. Manuf.* **2021**, *141*, 106221. https://doi.org/10.1016/j.compositesa.2020.106221.
18. Li, W.; Palardy, G. Investigation of welding repair methods for thermoplastic composite joints. *Compos. Part B Eng.* **2023**, *264*, 110924. https://doi.org/10.1016/j.compositesb.2023.110924.
19. Toray Advanced Composites. *Toray Cetex® TC1100 PPS Product Data Sheet*; Toray Industries, Inc.: Tokyo, Japan, 2021.
20. Toray Advanced Composites. *Toray Cetex® TC1225 LMPAEK™ Product Data Sheet*; Toray Industries, Inc.: Tokyo, Japan, 2023.
21. Lian, E. *Medium Toughness PAEK Thermoplastics Toray Cetex® TC1225 (LM PAEK) T700GC 12K T1E Unidirectional Tape 145 gsm 34% RC Qualification Material Property Data Report*; National Institute for Aviation Research, Wichita State University: Wichita, KS, USA, 2021.
22. *ASTM D5868-01*; Standard Test Method for Lap Shear Adhesion for Fiber Reinforced Plastic (FRP) Bonding. ASTM International: West Conshohocken, PA, USA, 2023.
23. Comer, A.; Katnam, K.; Stanley, W.; Young, T. Characterising the behaviour of composite single lap bonded joints using digital image correlation. *Int. J. Adhes. Adhes.* **2013**, *40*, 215–223. https://doi.org/10.1016/j.ijadhadh.2012.08.010.
24. Correlated Solutions. *VicPy API Documentation*; Correlated Solutions, Inc.: Irmo, SC, USA, 2024.
25. Kralovec, C.; Dengg, A.; Schagerl, M.; Schiller, A.; Bisagni, C.; Loebbecke, M.; Haubrich, J.; Hanelt, R. Static strength and fatigue life of pinned hybrid titanium-composite single-lap-shear joints. *Compos. Struct.* **2025**, *354*, 118765. https://doi.org/10.1016/j.compstruct.2024.118765.
26. Hart-Smith, L. *Adhesive-Bonded Single-Lap Joints*; NASA: Washington, DC, USA, 1973.